ACS OMEGA

Open Access

http://pubs.acs.org/journal/acsodf

Article

Reversible Wetting Transition of Water from Hydrophilic to Superhydrophilic State with UV-Ozone- and Ar-Plasma-Exposed Nanoporous Alumina Membranes: Microcooling, Sensing, and Filtering Applications

Saleem Shaik,* Prashant Kumar Gupta, Meenaxi Sharma, Krishnacharya Khare, and S. Anantha Ramakrishna

Cite This: *ACS Omega* 2025, 10, 17170−17181

Read Online

ACCESS | Metrics & More | Article Recommendations | Supporting Information

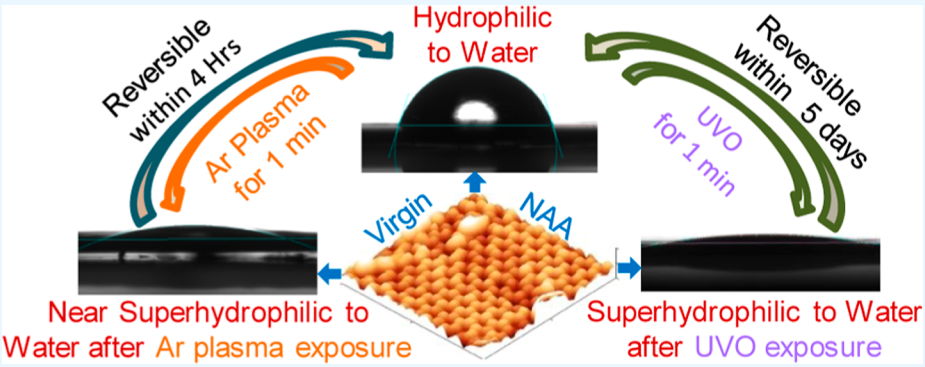

ABSTRACT: The hydrophilic−superhydrophilic transition dynamics of water on the multifunctional nanoporous anodic alumina (NAA) membranes of various pore lengths (0.03−5 μm) fabricated by the acid anodization process is demonstrated. The original pristine alumina surfaces were found to be in the hydrophilic Wenzel state. The pristine NAA sample surfaces were modified to a superhydrophilic state upon UV-ozone (UVO) exposure for 1 min. The sample surfaces were also modified to the near-superhydrophilic state by Argon plasma (Ar−P) treatment for 1 min. Carboxylate ions incorporated inside the NAA matrix during the anodization process were found to play an important role in modifying the sample surfaces to be superhydrophilic. It was revealed from XPS analysis that the increment in the oxygen percentage and reduction in the carbon percentage were the key points behind the superhydrophilic state after UVO and Ar−P treatment. The NAA matrix was made functional as a nanofluidic system consisting of water after UVO and Ar plasma exposure which can be used for micro-cooling, sensing, and filtering applications. Reversible switching to hydrophilic state was found, leaving the sample surfaces to ambient after UVO and Ar−P exposure.

INTRODUCTION

Wettability is a surface property which is determined by contact angle (CA) measurements, and in turn CA is mainly based on surface energy, chemical composition, and roughness of the surface.[1−3] So, CA and surface energy are related, as the higher the surface energy, the lesser will be the CA and vice versa.[3] To draw technical applications out of natural living systems, their wetting property should be understood. Topographic structures with controlled wettability can be shown by many living systems like lotus leaf, the compound eyes of mosquitoes, water striders, and geckos.[3] Surface wettability is considered as an important criterion that controls the biocompatibility of the implant and determines its long-term stability inside the human body.[1,3] Many methods have been developed to control the surface wettability of materials and devices by engineering the topographic structures of their surfaces, such as microfluidics, self-cleaning, anti-icing, biosensing, and filtration processes.[3,4]

Surface functionalization can be determined by the study of wetting properties.[5] The wetting properties of the surfaces are also influenced by surface roughness.[6] The fabrics made from porous materials can absorb water from the environment, possess pronounced texture and porosity, and also oriental plane capillarity along the threads.[5] Textiles showed hydrophilic behavior when varying the ambient gas nature and

Received: August 27, 2024
Revised: September 8, 2024
Accepted: September 12, 2024
Published: April 24, 2025

pressure inside the reaction chamber and hydrophobic nature when they were coated in vacuum with ZnO thin films and coated with nanoparticles with pulsed laser deposition.[7,8] ZnO nanostructures are also known for the ability to inhibit fungal development and to neutralize bacteria because of their wetting behavior.[9−14] Textile surface can be made hydrophobic by coating with SiO_2-sol with the added advantage of fine finishing.[15] Cotton fabrics exhibited flame-retardant properties when they were coated by silica nanoparticles after being immersed in silica suspension.[16] By coating TiO_2 nanoparticles on polyester/cotton fabrics, dual size surface roughness is created on the fabric, as the roughness is related to the geometry of the surface.[17] The wetting state on the surfaces of nanoporous and mesoporous structures was changed, which made the surface functionalize for specific applications by the post-treatment.[18−27] The interesting phenomenon of tunability in the pore sizes of the atomically thin graphene nanoporous oxide was demonstrated by Ar plasma and varying oxygen plasma treatment times.[28] Transition-metal oxides like ZnO, TiO_2, and V_2O_5 are known to change their wetting behavior to hydrophilic state upon UV exposure and transform to hydrophobic state on being stored in dark or by heat treatment.[29−31]

Apart from the nature of chemical bonds, the interactions of the surface with fluids can also be modified by structuring the surface. Nanoporous anodic alumina (NAA) is a structured surface whose nanopore topology can be modified in various manners,[33] and the alumina surface can be functionalized in various manners to make NAA superhydrophobic with amphiphilic compounds.[34] Even the manner in which NAA is prepared (the anodizing conditions) can influence the chemical species embedded in the surfaces of NAA. For example, the presence of the oxalate group within and on the alumina surface when oxalic acid was used for the anodization is well established.[35−32] Thus, NAA with a variety of wetting phenomena can be considered as a fertile ground for investigating various fundamental effects in this area.

The NAA structures were found to have great potential for producing surfaces with special wettability due to the controllable pore dimension and tunable surface chemistry. The Young CA of an intrinsic, smooth alumina surface was found to be about 85°.[41] However, combined with the specific surface structure and/or surface chemistry, superhydrophobicity and also superhydrophilicity have recently been achieved on NAA surfaces.[3,33,41−49]

NAA has been described to undergo transition from a Wenzel state to Cassie−Baxter state upon the increase of the nanopore size from 100 to 450 nm.[42] A similar Cassie to Wenzel state transition was observed as the pore length (L_p) was increased in NAA.[42] The Wenzel state is characterized by water moving into the nanopores and expelling the trapped air in small-diameter pores, and this expulsion of air also depends on whether pores are closed (thereby trapping the air) or opened,[43] while the Cassie and Wenzel states are two extreme situations where the fluid either does not enter or enters the nanopore, and intermediate states where the fluid partially enters the nanopore have also been reported.[44] Also considerable dynamics were involved when the initial contact angle of a droplet placed on NAA reduces over time to a small value due to the displacement of air from the nanopores which form air bubbles in the droplet.[41]

A variety of CA's have been reported in the literature on the prepared NAA, even for virgin surfaces, ranging from few degrees to 35° to over 85°.[41−43] These variety of CA's were measured for very similar morphology of NAA, and CA's ranging 65−85° are commonly reported for pristine NAA surfaces. The range of CA that was reported for pristine NAA surfaces is due to the high surface energy and highly hydrophilic nature of alumina. In the same context, in another work, CA was reported with a typical value of about 10−15° on α-Al_2O_3 for carboxylic acid and hydrophilic nanochannels of NAA for water.[33,45] Given that NAA also has the same chemical nature, a small CA is expected, at least for small nanopore sizes.

The dependence of surface wettability on the surface topography and the 3D structural parameters of the NAA membranes prepared under hard anodization were systematically investigated by Huang et al.[3] The roughness-dependent wettability was investigated systematically by varying L_p and the porosity of NAA films grown by a two-step anodization at a high voltage in phosphoric acid at three different concentrations independently, and as-grown NAA membranes were also synthesized after various degrees of pore opening by wet chemical etching.[46] The wettability of NAA was changed from hydrophilicity to hydrophobicity by increasing the pore diameter while maintaining the interpore distance and pore depth constant.[42] Superhydrophobic, fractal alumina surfaces without any chemical modification under high-field anodization in 0.3 M oxalic acid electrolytes were reported by Yao et al.[47] Alternatively, superhydrophobic surfaces were fabricated by either modifying the NAA surface using low surface energy materials or using NAA as a template for polymer synthesis. It was reported that NAA films with pore sizes in the range 10−80 nm can be transformed from being superhydrophilic to superhydrophobic by coating the surface with a thin (2−3 nm) layer of a hydrophobic fluoropolymer.[47] Superhydrophobic NAA membranes consisting of nanowire pyramids deposited on top of a nanoporous underlayer via high-field anodization in a 0.3 M oxalic acid solution were demonstrated.[48] Superhydrophilic NAA films with a strongly disordered structure were produced by Ye et al. in a single-step anodization in a 0.3 M phosphoric acid electrolyte in a galvanostatic mode.[49] Superhydrophilic NAA membranes with a bird's nest-like structure on top of a nanoporous layer were obtained from a single-step anodization procedure under a constant current in both phosphoric acid and oxalic acid solutions.[49] From all the above information, it can be concluded that NAA with varying pore geometries and surface modifications can change its surface chemistry; thereby, its wetting behavior can be tuned for various applications.

Another alternative method that was found to make the sample more hydrophilic or superhydrophilic is plasma exposure. Polystyrene micro-/nanopillars grew on mesoporous silica, and NAA showed transition between hydrophilicity to hydrophobicity and hydrophobicity to superhydrophilicity when they were treated by UV-O_3 (UVO) plasma, where it was reported that nanopillar arrays showed stable hydrophilicity as compared to micropillar arrays.[50] The C−C stretching in the vibrational spectra from the G-band in the Raman analysis and the formation of functional groups from CA measurements were shown by the UVO plasma-treated MWCNT array.[51] Reduction in the CA, increase in the surface reactivity, and a slight increase in the surface roughness were shown by oxygen plasma treatment on Si and SiO_2, and all these parameters are higher for Si than SiO_2.[52] Unlike oxygen plasma, which results in chemical etching by the degradation of

https://doi.org/10.1021/acsomega.4c07796
ACS Omega 2025, 10, 17170−17181

organic species and oxidation, it was reported that in addition to the change in surface chemistry, in general, Ar−P also results in physical etching by removing low-molecular-weight species except for few cases.[53] It was reported that the bombardment of Ar on the aluminum surface decomposes the Al−O bond of oxidized alumina; in addition, the bombardment of Ar may also cause the lattice distortion near the surface of aluminum.[54] Decrement in the CA to become a hydrophilic surface, increment in surface roughness, and surface energy on hydrophobic SU-8 gratings after Ar plasma exposure were reported by Zhang et al.[55]

In the present work, CA measurements of water droplets on NAA surfaces are presented. The virgin surfaces of NAA were prepared by anodization in oxalic acid, showing a CA of approximately 70°. Simply exposing NAA to UVO and Ar−P separately is seen to drastically reduce the CA to just about 10° (superhydrophilic) and 19° (near to superhydrophilic), similar to the case of pristine nonporous alumina.[33,45] It was observed that the CA, however, recovers to the previous large values over differing timescales in the two cases. The details of reduction and recovery are presented, and the reasons are attributed to the changes in the bonds or charge states of the surfaces. Here it is shown the necessity of having common starting point of a hydrophilic Al substrate to bring out the systematics of the contribution of hydrophilic pristine nanoporous alumina structures to the wetting transitions from hydrophilic to superhydrophilic and suggests simple techniques to improve the performances for the applications prescribed. A similar type of NAA was used as a nano-optofluidic refractive index sensor to detect 5% methanol in ethanol even without any UVO and Ar−P treatment.[56]

SAMPLE FABRICATION AND MEASUREMENT TECHNIQUES

The NAA samples were fabricated by anodizing a high-purity (99.999%, Thermo Fisher) Al foil in two steps at 40 V DC in a 0.3 M oxalic acid electrolyte[57] at about 3 °C [refer to the circuit diagram in Figure S1, Supporting Information]. Prior to anodization, samples were ultrasonicated in DI water and electropolished [refer to the mirror-finished Al in Figure S1, Supporting Information] in the mixture of 1:4 perchloric acid and ethanol to get the mirror-finished surface. Here, to study the wetting characteristics of water on the NAA surface of different L_p, the second step anodization time was varied. NAA samples with L_p of 0.03, 0.065, 0.25, 0.45, 0.65, 1.8, and 4.2 μm were fabricated corresponding to the anodization times of 7 s, 30 s, 5, 10, 15, 30, and 120 min, respectively, with a pore diameter (D_p) of about 40 nm. The schematic of the Al substrate and the various growth stages of NAA membranes' top and cross-sectional views, i.e., both pre-anodization and post-anodization of NAA prepared under the above conditions, are shown in Figure 1 with the 'Carl Zeiss' field emission scanning electron microscopy (FESEM) images. At the initial stages of NAA membrane growth (7 and 30 s) anodization times, we can observe pore initiation from the FESEM top view and cross-sectional images in Figure 1c−f. At the first step of pore initiation, i.e., at 7 s of second anodization, the vertices of the hexagonal matrix as the nucleation centers are shown in Figure 1c,e, and at this stage, the distance between the vertices is slightly large, and it is about 45 nm, and L_p is about 0.03 μm. In Figure 1c, a black background is shown which is nothing but the aluminum substrate. At this stage, only the barrier (pure oxide + contaminated oxide) type of oxide layer was formed; in general, its thickness is about 30−40 nm at the 40 V anodization condition.[58] In the second stage, at 30 s anodized aluminum, as shown in Figure 1d,f, the D_p is about 40 nm, and the L_p is about 0.065 μm. In this second stage, the formation of porous type of oxide started on the top of the barrier layer.[35−39,58]

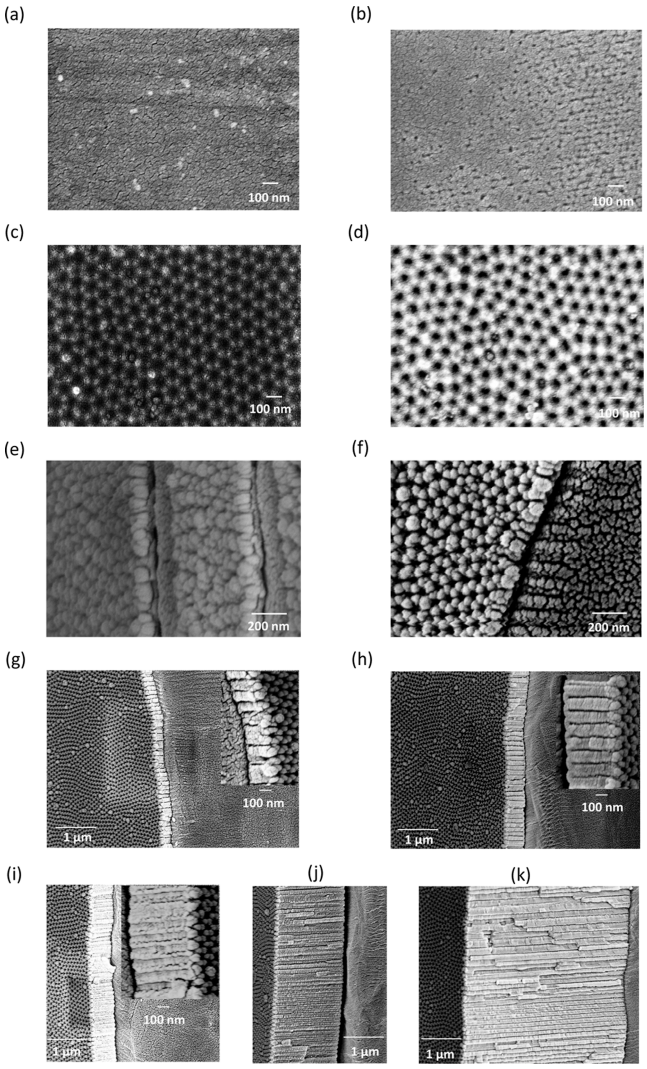

Figure 1. FESEM images of the aluminum substrate (a,b) top view before and after electropolishing, and NAA membrane (c,d) top view (at 7 and 30 s) and (e−k) cross section at 7 s, 30 s, 5, 10, 15, 30, and 120 min of second anodization.

The other five NAA membranes used in the main study of wetting dynamics are shown in Figure 1, with L_p of 0.25, 0.45, 0.65, 1.8, and 4.2 μm, prepared at second anodization conditions of 5, 10, 15, 30, and 120 min. For the first three samples with L_p of 0.25, 0.45, 0.65 μm, the zoom view is also shown in Figure 1g−i. Atomic force microscopy (AFM) measurements were also performed to analyze the surface roughness of plain aluminum before and after electropolishing and at several stages of nanoporous oxide growth by using Gwyddion software which in turn uses several statistical methods like autocorrelation Gaussian distribution function[59−61] [refer to the AFM analysis in Figure S2, Supporting Information]. The energy-dispersive spectroscopy (EDS) analysis (from Oxford Instruments Pvt., Ltd.) was also performed [refer to Figure S3, Supporting Information] to

https://doi.org/10.1021/acsomega.4c07796
ACS Omega 2025, 10, 17170−17181

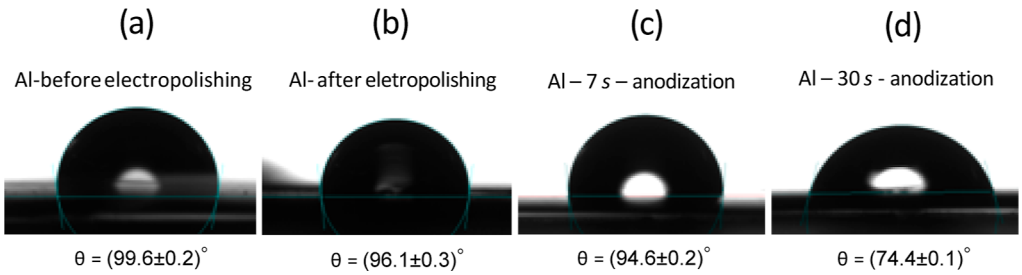

Figure 2. Schematic of CA measurement on an Al substrate (a) before and (b) after electropolishing and (c,d) after 7 and 30 s of second anodization on an electropolished Al substrate.

find the amount of oxide required for the reduction in CA value as compared to bare aluminum substrate. To alter the CA, samples were exposed to UVO (Advanced Curing System, Ind., Pvt., Ltd.) and Ar−P (Harrick Plasma extended, USA, with model no. PDC-002, PDC-FMG).

It is known that to find water wettability, CA measurements are necessary. For CA measurements, an "OCA 35" (Data Physics Instruments) goniometer was used. This device consists of a sample stage which can be moved along *X*, *Y*, and *Z* directions. The CA of a liquid drop on a solid substrate was measured after an image of the drop was captured with a CCD camera with 768 × 576 pixels and 40 frames per second. The measurement was carried out using software "SCA 20". In all of our measurements, the sessile drop method was used.

RESULTS AND DISCUSSION

Contact Angle Measurements of DI Water on the NAA Surface at the Initial Stages of Pore Formation. The study of wetting dynamics of water before (pre-anodization) and just after (initial stages of post-anodization) oxide formation is considered very crucial to understand the wetting dynamics of water after the full growth of nano-structured NAA membranes. A water droplet of 4 μL was gently loaded on the sample surface in all of our experiments by using a goniometer. Initially, the CA measurements were performed on the aluminum substrate, which was supplied as it is. The CA measured was about 99.6°, as shown in Figure 2a. The same substrate was electropolished, and then CA whose value is about 96.1° is measured, as shown in Figure 2b. The difference in CA, as shown in Figure 2, before and after electropolishing (pre-anodization condition), is due to the reduction in surface roughness after electropolishing [refer to the AFM analysis in Figure S2, Supporting Information]. From this figure, it can be observed that the surface undulations on the bare Al substrate before electropolishing were reduced, and it is also the reason behind the uniform growth of porous structures. After electropolishing, the two-step anodization procedure was performed as discussed in the Sample Fabrication and Measurement Techniques section for 7 and 30 s. After 7 s of second anodization on the same sample with the L_p value of about 0.03 μm, only pure aluminum oxide was formed on the textured surface of the electropolished sample [refer to the AFM analysis in Figure S2, Supporting Information and Figure 1 for FESEM]. The CA measurements were repeated on the same sample, whose value is about 94.6° as shown in Figure 2c, which is 5° lesser than the CA measured on the aluminum substrate. After this stage, the same sample was anodized for 30 s where the L_p value is about 0.065 μm [refer to the circuit diagram in Figure S1, Supporting Information], and then the CA measurements were repeated again. Here, the CA value was reduced to 74.4° as shown in Figure 2d. From the FESEM images of Figure 1c−f and AFM and EDS studies [refer to Figures S2 and S3, Supporting Information], it is observed that in the transition from the pore initiation (7 s anodization) to proper porous oxide growth (30 s anodization), although the surface roughness of the sample increased the CA reduced as the system is presumably in the Wenzel state. So, the CA value was reduced from 96.1° to 74.4°, just for 7−30 s of anodization, which is significant. So, it can be concluded that as soon as the barrier type of oxide formation starts on the sample surface, the CA value starts decreasing, although not to the small values expected of a pristine α-Al_2O_3 hydrophilic surface.

Hydrophilic−Superhydrophilic Transition of DI Water on the NAA Surface after UV-O_3 Exposure. To understand the wetting dynamics of water on NAA, a set of five samples with L_p ranging from 0.25 to 4.5 μm were fabricated as shown in the FESEM images of Figure 1g−k. The set of CA measurements was taken on five samples at different locations on their surfaces.

The plot of CA versus L_p of NAA for five samples is shown in Figure 3. From the plot in Figure 3 (black curve) before UVO, it can be observed that for NAA with a L_p of 0.25 μm, the contact angle is about 68° with a standard deviation (SD) of about 2°, which is less than Young's CA (θ_y = 85°)[41] for the planar virgin alumina surface. For NAA with a L_p of 0.45 μm,

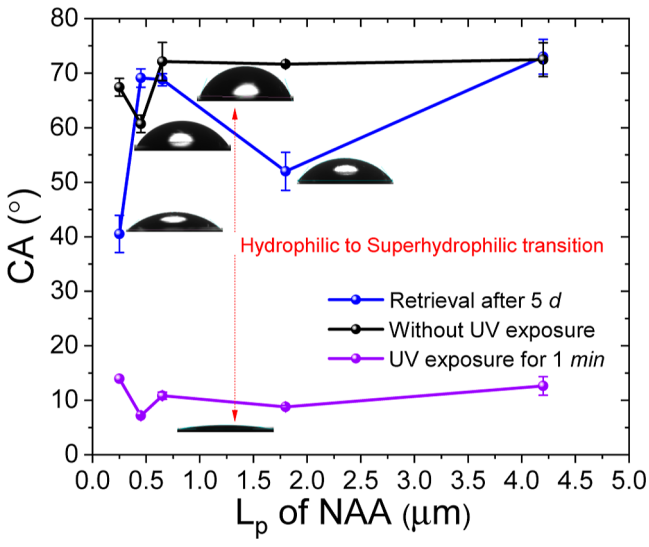

Figure 3. Average CA vs L_p of NAA corresponding to the second anodization time (5, 10, 15, 30, and 120 min), before (black curve) and after (violet curve) UVO exposure for 1 min and retrieved after 5 days (blue curve).

https://doi.org/10.1021/acsomega.4c07796
ACS Omega 2025, 10, 17170−17181

the CA is reduced to 60° with a SD of about 2°. This is the minimum CA observed for the virgin surfaces. Similarly, the CA was measured on three NAA samples with L_p of 0.65, 1.8, and 4.2 μm, which is about 70° with a SD of 2° slightly higher than the CA for NAA with a L_p of 0.25 μm [refer to Figure S4a−e, Supporting Information, in the Ar−P exposure section]. After UVO (at λ_1—184.9 nm, λ_2—253.7 nm) exposure for 60 s, in an oxygen atmosphere, the CA values reduced significantly, as all the NAA samples were almost found in the superhydrophilic state and have a CA of about 10° [refer to Figure S4f−j, Supporting Information, in the UVO exposure section and in Figure 3 with a violet curve]. The CA of 7.3° on NAA with a L_p of 0.45 μm, as shown in Figure 3 with a violet curve [refer to Figure S4g, Supporting Information, in the UVO exposure section], was found out to be a superhydrophilic state as it is <10°. After 5 days of UVO exposure on pristine alumina surfaces, the CA values of samples were recovered to about 70° when left in an ambient atmosphere for 5 days as shown in the plot (Figure 3, blue curve) with a SD of about 5° [refer to Figure S4k−o, Supporting Information, in the UVO exposure section].

All these CA's were measured less than Young's CA (θ_y = 85°)[41] for the planar virgin alumina surface and are all expected to be in the Wenzel state. It can be explained as follows: for the given liquid volume of 4 μL nanopores in the case of NAA samples with L_p of 0.25, 0.45, and 0.65 μm cofilled because of the capillary force, the droplet makes higher CA's (about 67° and 70°) in the first and third samples as compared to the second sample which is about 60°.

In the case of NAA with L_p of 1.8 and 4.2 μm, the penetration path (the hollow pores until the bottom) for the flow of the liquid droplet is not opened fully even though the capillary force acts, unlike NAA with L_p of 0.25, 0.45, and 0.65 μm. So, most of the liquid volume lies on the surface of NAA with L_p of 1.8 and 4.2 μm, and hence, the CA value is not reduced.

Hydrophilic−Near-Superhydrophilic Transition of DI Water on the NAA Surface after Ar−P Exposure. To verify the discussion in the previous section, the pristine NAA surfaces were exposed to Ar−P as well, which would also clean up the surface. As a surprise, the CA was reduced here too, although the extent of reduction was slightly smaller: the CA was about 17° as shown by the plot in Figure 4 with a red curve, where the surface did not become superhydrophilic [refer to Figure S5f−j, Supporting Information, in the Ar−P exposure section]. Further, when this Ar^+-treated surface is kept exposed to the ambient atmosphere, the recovery of the CA occurred over much shorter times of few hours compared to several days in the case of the UVO exposure. This can be understood by noting that NAA is quite insulating and that the surface would become charged by exposure to Ar−P as well. This charged surface would indeed become hydrophilic and wettable for a polar liquid like water, but the charge volatilizes and the surface becomes neutral rather fast in an ambient atmosphere.

The same set of CA measurements was repeated on the other similar (as that of the UVO case) set of five samples at different locations here as well, as shown in Figure 4, and the black curve is without any exposure. The CA value on NAA with a L_p of 0.45 μm is 68° with a SD of 5° and on NAA with L_p of 0.25, 0.65, 1.8, and 4.2 μm, the CA value is about 70° with a SD of 5° [refer to Figure S5a−e, Supporting Information, in the Ar−P exposure section]. The CA

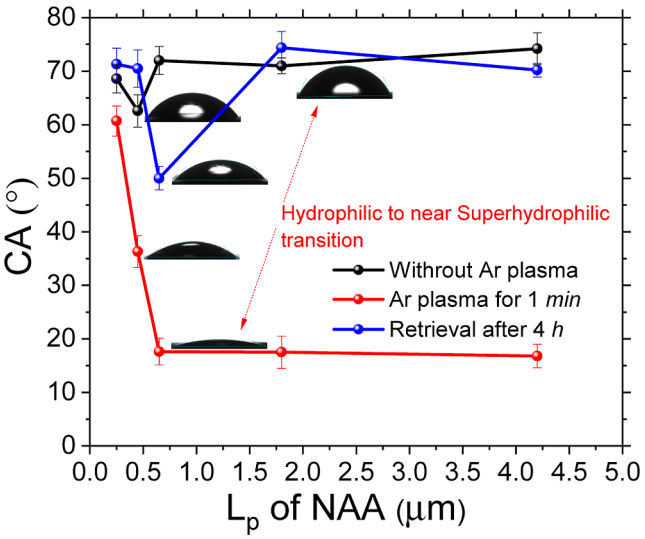

Figure 4. Average CA vs L_p of NAA corresponding to the second anodization time (5, 10, 15, 30, and 120 min) before (black curve) and after (red curve) Ar−P exposure for 1 min and retrieved after 4 h (blue curve).

measurements were taken even after Ar−P exposure for 1 min Figure 4 (red curve). It was found that for NAA with a L_p of 0.25 μm, the CA reduces from 70 to 60°, and for NAA with a L_p of 0.45 μm, the CA reduces from 65 to 35°, and for the remaining three samples with L_p of 0.65, 1.8, and 4.2 μm, the CA reduces to 19° with a SD of 5° after Ar−P exposure. The retrieval in the CA is found within 4 h, which is shown in Figure 4 blue curve with a CA of 50° on NAA with a L_p of 0.65 μm and a CA of 70° on the remaining four samples. Thus, with the Ar−P exposure, superhydrophilic states (CA < 10°) were not obtained as with the UVO exposure. After 4 h of Ar−P exposure (for 1 min), CA recovery was observed to be almost the same as that of original, except for the NAA sample with a L_p of 0.45 μm [refer to Figure S5f−j, Supporting Information, in the Ar−P exposure section and the plot (Figure 4, blue curve)]. The CA measured for NAA with a L_p of 0.65 μm is 50°, and for the remaining sample, it is about 71° [refer to Figure S5k−o, Supporting Information, in the Ar−P exposure section].

Calculation of the Penetration Depth of Water in the Nanopores of Virgin NAA Membranes. The liquid volume remaining (V_r) on the sample surface (or volume of the spherical cap) was calculated by using the formula

$$V_r = (\pi h/6)(3r^2 + h^2) \quad (1)$$

where r is the radius of the circle and h is the height of the water droplet on the sample surface. The r and h values for the five NAA samples with L_p of 0.25, 0.45, 0.65, 1.8, and 4.2 μm are shown in Figure 5a−e. V_r on the sample surface was calculated to be 3.7, 3.6, and 3.1 μL, and in the remaining 1.8 and 4.2 μm samples, it is about 3.2 μL.

The amount of liquid volume (V_p) filled inside the pores is calculated by subtracting V_r from the total volume (V_T = 4 μL) of the liquid droplet placed on the sample surface

$$V_p = V_T - V_r \quad (2)$$

The pores of NAA with L_p of 0.25, 0.45, and 0.65 μm were filled by water with a volume (V_p) of 0.3 μL, 0.4 μL, and 0.9 μL, and in the remaining samples, it is only 0.8 μL.

https://doi.org/10.1021/acsomega.4c07796
ACS Omega 2025, 10, 17170−17181

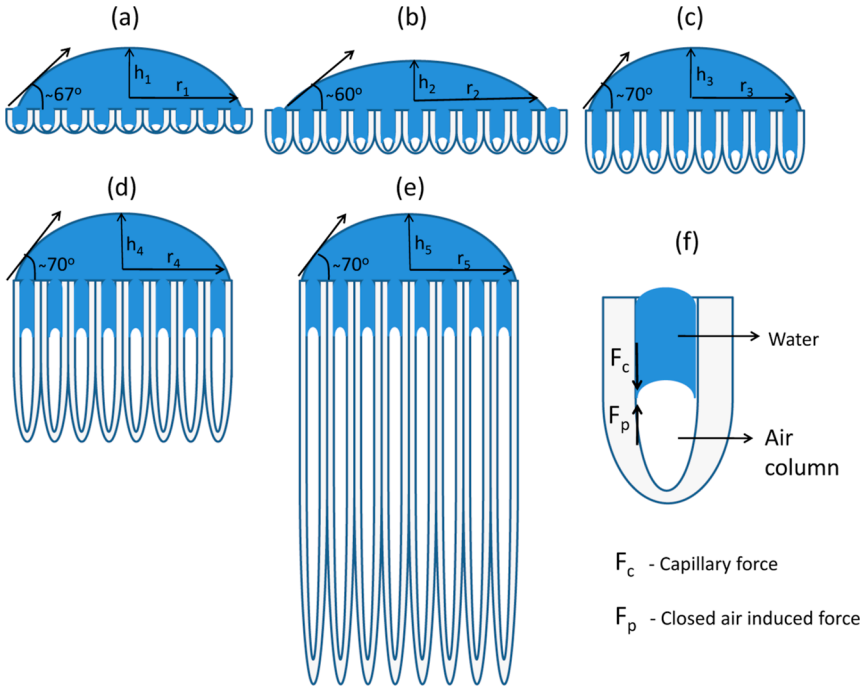

Figure 5. Schematic model of water penetration into the pores of NAA with L_p of (a−e) 0.25, 0.45, 0.65, 1.8, and 4.2 μm, where (r_1, h_1), (r_2, h_2), (r_3, h_3), (r_4, h_4), and (r_5, h_5) were measured to be (1.45, 0.97 mm), (1.5, 0.91 mm), (1.34, 0.93 mm), (1.36, 0.95 mm), and (1.36, 0.95 mm); (f) balance between capillary and closed air-induced forces.

The capillary force is related to d_p and Young's CA[62]

$$F_c = \pi\gamma d_p \cos\theta_y \quad (3)$$

where d_p is the pore length, γ is the surface tension (72 mN/m) of water, and θ_y is Young's CA of water droplet on the NAA surface.

The pressure induced by the trapped air against water penetration into the pores is[42]

$$F_p = P_o H\pi d_p^2/4(L_p - H) \quad (4)$$

where P_o is the atmospheric pressure (1.013×10^5 N/m^2), L_p is the pore length, and H is the penetration depth.

These two forces oppose each other, and balancing the equation leads to the pressure balance equation; thereby, the penetration depth (H) can be calculated. The schematic of the balance between the capillary force (F_c) and the pressure ((F_p)) due to the closed air inside the pores is shown in Figure 5f.

$$H = L_p\left[1 + \frac{P_o d_p}{4\gamma \cos\theta_y}\right]^{-1} \quad (5)$$

The H values calculated by eq 5 for NAA with L_p of 0.25, 0.45, 0.65, 1.8, and 4.2 μm are 0.215, 0.387, 0.560, 1.55, and 3.61 μm under ideal conditions when the pores are fully opened until the bottom. Under these ideal conditions, the CA values should be reduced as the H value increases. However, from the CA variation which was shown by the black curve in Figure 3, it is clear that the CA values become constant (about 70°) for NAA with L_p of 0.650, 1.8, and 4.2 μm.

To understand this, a model is designed as shown in Figure 5 which is based on CA values measured at one instant [refer to Figures S4a−e and S5a−e, Supporting Information]. It can be observed from Figure 5a−c that for the first three samples with L_p of 0.25, 0.45, and 0.65 μm, the water droplet wets the pores almost until the bottom with small closed air gaps with H values of 0.215, 0.387, and 0.560 μm, as the pores are opened. However, after reaching the critical L_p of 0.65 μm, the CA increased to 70°, as shown in Figure 5c, as compared to the first two samples with L_p of 0.25 and 0.45 μm with CA values of about 60 and 67°. Even though the CA value was increased to 70° for NAA with a L_p of 0.65 μm, from 1 it is clear that the V_r value is 3.1 μL, which is the least among the five samples. So, it is clear that water penetrated deep into the pores until 0.560 μm in NAA with a L_p of 0.65 μm. In the remaining two samples with L_p of 1.8 and 4.2 μm, the CA values are almost the same as that of the sample with a L_p of 0.65 μm, as shown in Figure 5c−e, and the surface roughness values for these last three samples are almost constant. Further, V_r and V_p of the last three samples are almost the same as shown in Figure 5c−e as the CA values are almost the same. Hence, it can be concluded that the H values of water inside the pores of NAA become almost constant for the three samples with L_p of 0.650, 1.8, and 4.2 μm, as shown in Figure 5c−e, and the reason is that after certain L_p, the penetration path for water becomes narrower; thereby, F_v opposes F_c, as shown in Figure 5f.

X-ray Photoelectron Spectroscopy Analysis of NAA Membranes before and after UVO and Ar−P Exposure. The as-fabricated NAA matrix was found consisting of several impurities [refer to the circuit diagram in Figure S1, Supporting Information]. These impurities are carboxylate ($C_2O_4^{2-}$) and mono-oxalate (COO^-) ions that were embedded inside the outer layer and the middle layer of the NAA porous structure during the anodization process, and the inner pure aluminum oxide layer is just above the aluminum (Al)-textured substrate.[35−39] The wetting dynamics of the NAA membrane are greatly influenced by these impurities.

After UVO exposure for 60 s [refer to Figure S4f−j, Supporting Information, and Figure 3, violet color curve), the

https://doi.org/10.1021/acsomega.4c07796
ACS Omega 2025, 10, 17170−17181

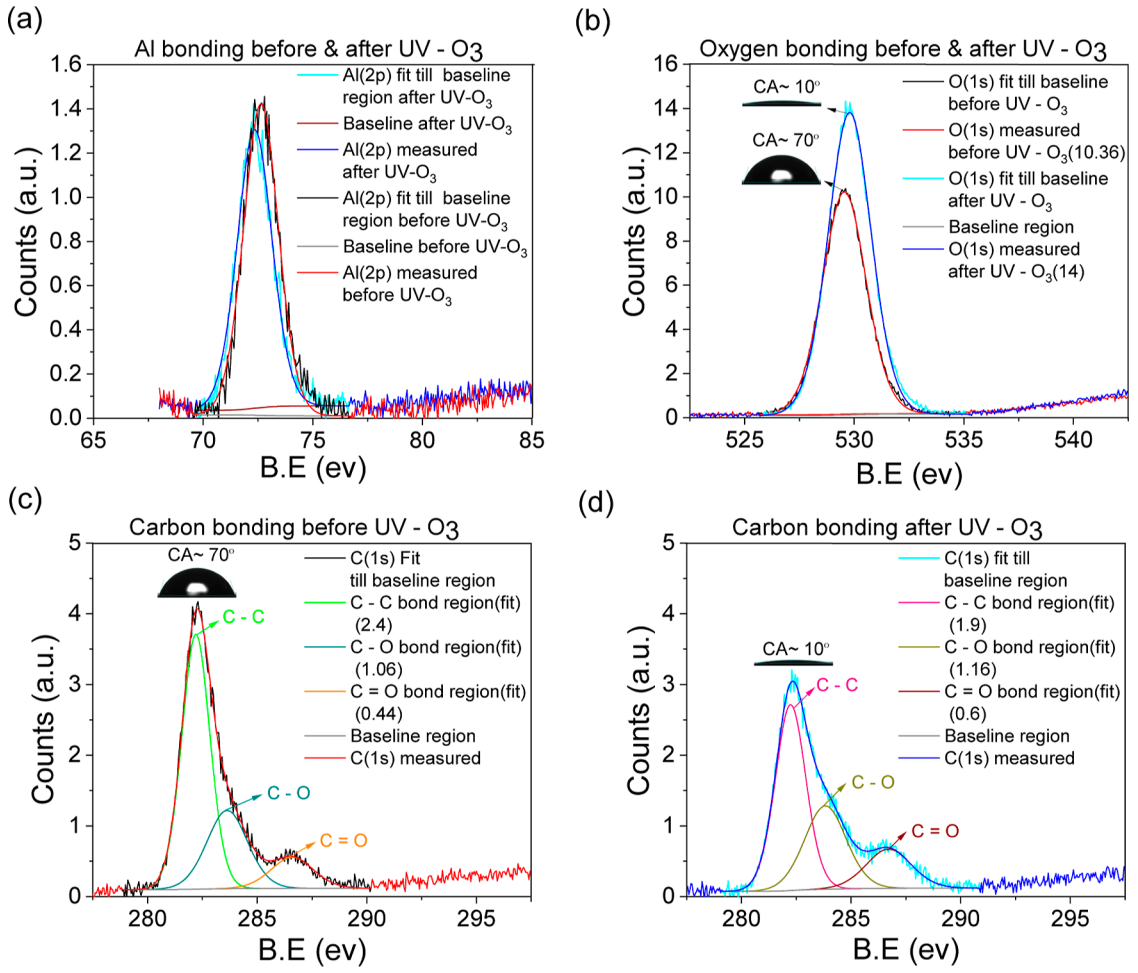

Figure 6. XPS analysis of (a) oxygen, (b) aluminum, and (c,d) carbon ions present on the NAA surface before and after UVO exposure.

CA of the water droplet on the NAA surface was reduced significantly. It can be explained as follows: the oxygen ions form bonds on the NAA surface with Al; thereby, it is oxidized. This reduction of the CA and the increased wettability may be understood by noting that ozone formed under the ultraviolet light would oxidize the surface, leaving the surface of NAA decorated by OH bonds and reducing the surface energy. Consequently, the surface becomes highly wettable by a polar liquid like water. Quite interestingly, when left in the ambient atmosphere, the OH bonds volatilize over time, leaving the surface in the same state as before, and the large CA's are once again recovered. To confirm this and to understand deeply the CA behavior of water on the NAA surface before and after UVO treatment, it was characterized by XPS. In the XPS analysis, the aluminum counts (area under the curve) after (blue curve) and before (red curve) UVO exposure at 72.5 eV binding energy (BE) were observed to be constant, as shown in Figure 6a. The Al amount was found constant throughout the XPS measurements, and in all of our XPS analyses, the averaged area under the curve (245.6) of the Al peak before and after UVO exposure was taken as constant and as a reference.

It was observed that after UVO exposure, the overall oxygen percentage on the NAA surface is increased, as shown in Figure 6b after (blue curve) and before (red curve) UVO exposure at BE about 528 eV. It is known that in nature oxygen always forms bonds with the surrounding entities, and hence, the increment in O_2 percentage is actually the increment in Al_2O_3 percentage. After UVO treatment, because of the moisture in the atmosphere, OH bonds are formed as well. So, the oxygen 1s orbital peak, as shown in Figure 6b, was normalized with the averaged Al percentage (Al 2p orbital) as shown in Figure 6a. It was normalized in this way: initially, the area under the curve of the oxygen peak, before (red curve−−2545.4) and after (blue curve−−3433.4) UVO exposure, separately, was divided with the averaged area under the aluminum peak in the XPS analysis; thereby, it is confirmed that the oxygen percentage is more in the UVO-exposed NAA sample. It was found that the increment in the oxygen percentage is from 10.36 to 14 after normalization. Here, the CA value decreased from 70 to 10° with the increment in oxygen percentage, as shown in Figure 6b.

The reduction in the carbon percentage is also confirmed through XPS characterization, as shown in Figure 6c,d, indicated with the measured curve before (red) and after (blue) UVO exposure. In Figure 6c,d, the measured curve was fitted and split into C−C, C−O, and C═O bond regions indicated with green, cyan, and orange curves before UVO exposure and with magenta, dark yellow, and brown colors after UVO exposure at BEs of 284.4, 285.8, and 288.3 eV, respectively, but here there is an increment in C−O and C═O bonds after UVO exposure. The oxalate ions were embedded in the outer layer of the NAA surface during anodization

https://doi.org/10.1021/acsomega.4c07796
ACS Omega 2025, 10, 17170−17181

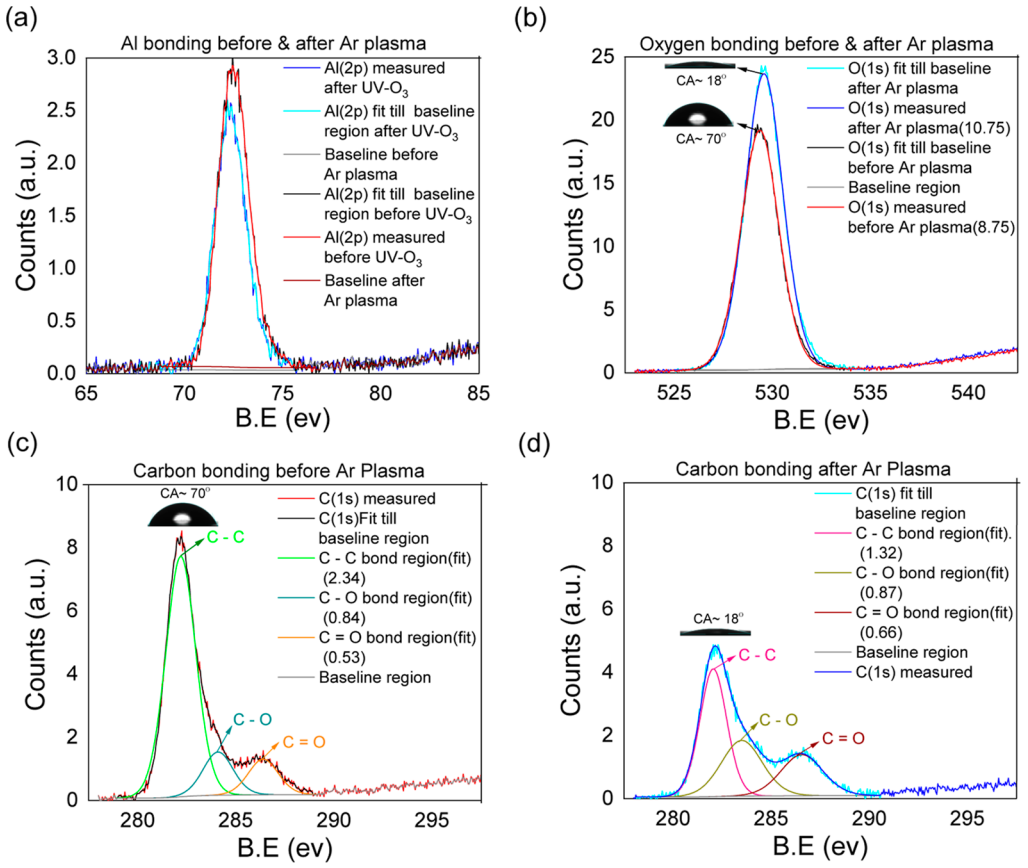

Figure 7. XPS analysis of (a) oxygen, (b) aluminum, and (c,d) carbon ions present on the NAA surface before and after Ar−P exposure.

because of electrochemical reactions, as well as in the middle layer.[35−39]

It is known that the major wavelengths of the ultraviolet rays radiated from a well-known low-pressure mercury vapor lamp are 184.9 and 253.7 nm,[63−65] where the energy (E) per mole of ultraviolet rays with a wavelength of 184.9 nm is 647 KJ/mol, and for 253.7 nm, it is 472 kJ/mol. When atmospheric O_2 is exposed to ultraviolet rays with a wavelength of 184.9 nm, oxygen absorbs the ultraviolet rays to form ozone (O_3), and then O_3 exposed to ultraviolet rays with a wavelength of 253.7 nm absorbs the ultraviolet light to decompose O_3.[63−65] During this process, atomic oxygen (O) with a strong oxidizing ability is generated.[63−65] If any surface containing organic compounds is irradiated with UV rays with energy stronger than the bond dissociation energy, then photolysis occurs due to the absorption of UV rays; as a result, ions, free radicals, and excited and neutral molecules are formed.[63−65] These excited molecules, ions, and free radicals of the contaminants can be reacted with atomic oxygen to form molecules such as CO_2,H_2O, N_2, and O_2, which are removed from the surface.[63−66] As discussed in the Sample Fabrication and Measurement Techniques section, the $C_2O_4^{2-}$ and COO^- contaminants were formed during the anodization process of NAA, and the corresponding bond dissociation energies of C−C C−O, and C═O bonds are 347.7, 351.1, and 724 kJ/mol, respectively.[67] So, by comparing the bond dissociation energy values of UV rays and the contaminants in NAA membranes, it can be confirmed that UVO exposure is sufficient to break the bonds of C−C in $C_2O_4^{2-}$ ions; thereby, the carbon contaminants left after dissociation react with oxygen and form CO_2 which mixes with the outer atmosphere through the outlet.

After the breakage of these bonds, the partial double bonds between C and O, i.e., C═O, will be much stronger because of the increase in electronegativity. Now, after this action, it is possible that some of the carbon escapes from the NAA surface in the form of carbon dioxide (CO_2); thereby, the reduction in the carbon percentage is confirmed through XPS characterization as shown in Figure 6c,d, indicated with the measured curve before (red) and after (blue) UVO exposure. In the same curve, it can be observed that the small peak has a slightly higher binding energy, which is at 288.3 eV, and it corresponds to the C═O bond, but here, there is an increment after the UVO exposure. For confirming the bonding information, the theoretically fitted curve was split into three components. The first component is C−C (at 284.4 eV), the second is C−O (at 285.8 eV), and the third is C═O bond (at 288.3 eV), which are the best fits, as shown in Figure 6c,d, before (green, cyan, and orange curves) and after (magenta, dark yellow, and brown curves) UVO exposure. It can be observed that there is an increment in the C−O and C═O bond percentage after UVO exposure contrary to the C−C bond case; the percentage reduction in C−C is from 61.5 to 52, and the percentage increment in C−O and C═O is from 27.20 to 31.8 and 11.32 to 16.28. Here, the CA is decreased from 70 to 10° with a reduction in C−C bonding, as shown in Figure 6c,d. Further, the area under the curve of C−C, C−O, and C═O, as shown in Figure 6c,d, was normalized with the area under the curve of Al bonding (Figure 6a) before and after UVO exposure, in the same way as that of the oxygen bonding case. The area under the curve for C−C, C−O, and C═O before and after UVO

https://doi.org/10.1021/acsomega.4c07796
ACS Omega 2025, 10, 17170−17181

exposure was measured to be about 590.7, 261.3, 108.8, and 466.6, 285.7, and 146.3, respectively. After normalization with Al, the decrement in the C−C bond factor is found to be from 2.4 to 1.9, and the increment in C−O is found to be from 1.06 to 1.16 and that of C═O is from 0.44 to 0.6. After Ar−P exposure for 60 s [refer to Figure S5f−j, Supporting Information, and Figure 4, red color] the CA's of the water droplets on the NAA surfaces were also reduced significantly. It can be explained as follows: the surface radicals formed on the surface form bonds with oxygen after the sample is removed from the plasma chamber. To confirm this, the NAA surfaces were characterized before and after Ar−P exposure with XPS again. In the XPS analysis, it was observed that the aluminum percentage is constant after (blue curve) Ar−P and before (red curve) Ar−P exposure, which is shown in Figure 7a at a BE of 72.5 eV. Here also, Al was considered as a reference by taking the averaged area (532.65) under the curve of Al peak before and after UVO exposure.

It was observed that after Ar−P exposure also, the overall oxygen percentage on the NAA surface increased, which is shown in Figure 7b at a BE of 528 eV, which is actually the increment in the Al_2O_3 percentage. So, the oxygen 1s orbital peak, as shown in Figure 7b, was normalized with the Al percentage (Al 2p orbital), as shown in Figure 7a. Here also, the area under the curve of the oxygen peak, before (red curve−−4663.3) and after (blue curve−−5749) Ar−P exposure, was divided with the averaged area under the curve of the aluminum peak in the XPS analysis, separately; thereby, it was confirmed that the oxygen percentage is more in the Ar-exposed NAA sample. It was found that the increment in the oxygen percentage is from 8.8 to 10.8 after normalization, but this is less than that of the UVO case. Here, the CA value is decreased from 70° to 18° with the increment in oxygen percentage, as shown in Figure 7b.

Here, a much more reduction in carbon percentage as compared to the UVO case was observed, which is confirmed through XPS characterization, as shown in Figure 7c,d, indicated with the measured curve before (red) and after (blue) Ar−P exposure. In Figure 7c,d, the measured curve was again fitted and split into C−C, C−O, and C═O bond regions indicated with green, cyan, and orange curves before Ar−P exposure and with magenta, dark yellow, and brown colors after Ar−P exposure at BEs of 284.4, 285.8, and 288.3 eV, respectively, but here also, there is an increment in C−O and C═O bonds after Ar−P exposure.

A large number of energetic species including free radicals, electrons, ions, and excited molecules can be engendered even by Ar−P exposure, which leaves stable radicals on the surface for later reactions in the ambient atmosphere. However, being an inert gas process, Ar−P effectively changes the surface chemistry.[68] Apart from the change in surface chemistry in some cases, Ar−P also changes the physical geometry; in the current scenario, however, any change in the surface topography locally due to the change in the pore size of NAA membranes has not been taken into consideration as the power chosen to operate the plasma was not enough to physically etch the surface. Power was adjusted in such a way that it was enough to activate the surface without any physical etching. Also, it was reported earlier that the plasma treatment of 60 s on an ultrathin Au film did not significantly alter the surface roughness.[69]

In the present scenario, the Ar−P exposure was operated under an RF power of 7.2 W and a frequency of 3.5 MHz due to the ionization of Ar atoms. In the chamber with argon gas at such low pressure, when the NAA substrate is placed on an unbiased substrate, it is evident that there will be highly energetic electrons because of the nonequilibrium nature of the plasma; at the same time, the energy of the ions and neutrals will be near to the room temperature (0.025 eV),[70] but this ion energy is not sufficient to break the C−C bonds. When the ions were hit by the electrons inside the chamber, they lose a small fraction of energy (mass of the electron/mass of the proton), and in this process, they continue to gain energy as well. Due to the above facts, it can be assumed reasonably that the changes in the surface are because of the energetic electrons and not due to the low-energy ions.

The high energetic electrons in Ar−P were considered responsible for the breakage of the C−C bonds in $C_2O_4^{2-}$ (carboxylate ions) on the surface of NAA; thereby, a great reduction in carbon percentage is observed as compared to the UVO case, as shown in Figure 7c,d, indicated with the measured curve before (red) and after (blue) Ar−P exposure. After the breakage of these bonds, the partial double bonds between C and O, i.e., C═O, will be stronger because of the increase in electronegativity. The carbon contaminants may react with atomic oxygen to form simple molecules such as CO_2 and were sent outside through an outlet at the end of the process. In the same curve, it can also be observed that the small peak is at a slightly higher binding energy, which is at 288.3 eV, and it corresponds to the C═O bond, but here, there is an increment after Ar−P exposure. For confirming the bonding information, the XPS-measured curve was theoretically fitted where it splits the entire curve into three components. The first component is C−C (at 284.4 eV), the second is C−O (at 285.8 eV), and the third is C═O bond (at 288.3 eV) which are the best fits, as shown in Figure 7c,d, before (green, cyan, and orange curves) and after (magenta, dark yellow, and brown curves) Ar−P exposure. It can also be observed that there is an increment in the number of C−O and C═O bond percentage after UVO exposure contrary to the C−C bond case. It is observed that the percentage reduction in C−C is from 63.03 to 46.16, and the percentage increments in C−O and C═O are from 22.64 to 30.7 and 14.33 to 23.1. It was found that the difference in percentages is more than that in the UVO case. Here, the CA decreased from 70 to 18° with a reduction in C−C bonding, as shown in Figure 6c. Further, the area under the curve of C−C, C−O, and C═O, as shown in Figure 7c,d, was normalized with the area under the curve of Al bonding (Figure 7a) before and after Ar−P exposure, in the same way as that of the oxygen bonding case. The area under the curve for C−C, C−O, and C═O before and after UVO exposure was found out to be about 1250.3, 449.2, 284.3, and 707.2, 468.2, and 354.9, respectively. After normalization with Al, the decrement in the C−C bond factor is found to be from 2.34 to 1.32, and the increment in C−O is found to be from 0.84 to 0.87 and that of C═O is from 0.53 to 0.66.

It is also clearly found from the XPS data, as shown in Figure 7b, that there is an increase in the oxide group after Ar−P exposure, which indicates the enhanced surface reactivity, such as oxidation in the presence of air. Thus, it is made clear that the oxygen species increased markedly after Ar plasma exposure. Therefore, inclusion of the polar hydroxyl group and oxide group on the treated surface was found by Ar−P exposure; thereby, the surface energy of NAA after being exposed to Ar−P would be higher compared to that of the untreated surface. Reduction of the hydrocarbon species and

https://doi.org/10.1021/acsomega.4c07796
ACS Omega 2025, 10, 17170−17181

introduction of hydroxyl and oxide groups were found to be the primary factors that increase the hydrophilicity of the NAA surface after Ar−P exposure.

While obtaining hindsight into the increase of wettability of the UVO- or Ar−P-treated NAA surfaces, here, the original anodized surfaces were measured with large CA's. This would necessarily emanate from the chemical state of the surface. NAA formed by anodization in oxalic acid is well known to incorporate oxalate and even carboxylate ions into and on the matrix.[35−39] Photoluminescence from such NAA surfaces is known to emanate from oxalate impurities. The surface wettability can be reduced by such organic impurities. The interesting thing here is that the CA was recovered again over time after exposing NAA samples (both UVO- and Ar−P-treated) to the open atmosphere as surface charges and ions might have been volatilized over time. In one earlier work, the NAA surface was washed by tap water (containing chloride ions) instead of deionized water (as is the case here).[41] The surface was found in a superhydrophilic state with CA's of about 8° by loading the surface with the water droplet containing chloride ions.[41] This effect is rather permanent, as the chloride ions cannot be volatilized easily.

CONCLUSIONS

The wetting dynamics study of 4 μL water droplets on the aluminum substrate before and after anodization revealed the fact that in the latter case after barrier layer formation on NAA, the CA reduces due to the reduction in surface roughness. The higher L_p pristine NAA surfaces (0.25−4.2 μm) were found in the Wenzel hydrophilic state. Upon UVO exposure, these sample surfaces become superhydrophilic. The near-superhydrophilic state was also observed upon Ar exposure on the same set of pristine NAA surfaces.

From the CA measurements of DI water on the NAA samples, it can be concluded that the UVO effect lasts a long time on NAA samples as compared to the Ar−P treatment. This is due to the fact that in the former case the tendency of oxygen bond formation is more, thereby more OH^- ions, as UVO was used in ambient, whereas in the latter, even though the reduction in carbon percentage is huge, the tendency of oxygen bond formation is less since it is in vacuum, and even after the removal of the sample from the vacuum chamber and exposure to the open atmosphere for about 5 min, the percentage increase in OH^- ions is less. The CA values were recovered within 5 days in the UVO case and within 4 h in the case of Ar−P after leaving samples to the ambient, which is also an interesting and significant finding out of this study.

Thus, it can be concluded that the wetting nature of the NAA surface depends enormously on the charges and bonds on the surface. With this study, it can also be concluded that the post-anodization treatment can significantly enhance the wettability of the NAA surface. It is noted in hindsight that the samples considered here would all be in the Wenzel state, where water enters the nanopores and the surface would significantly enhance the wettability. Increasing the wettability and making the surface superhydrophilic have very important consequences for evaporative cooling applications, particularly for microcooling applications and filtering applications where NAA can be fit as an important candidate among the various materials. In an earlier work, similar pristine NAA membranes with widened pores were used for alcohol sensing applications to find toxic elements like methanol in ethanol.[56] In a similar manner, NAA with UVO and Ar−P exposure for 1 min can also be readily used as a nano-optofluidic refractive index sensor to find contaminants inside water by making the pores of NAA open throughout by implementing a pore-widening step for water circulation.

ASSOCIATED CONTENT

Supporting Information

The Supporting Information is available free of charge at https://pubs.acs.org/doi/10.1021/acsomega.4c07796.

Electropolishing and anodization of the Al substrate to understand the origin of oxalate ions; AFM analysis of Al substrate and NAA membranes of various L_p; EDS analysis of NAA membranes of various L_p; CA measurements of water on UVO-exposed NAA membranes; and CA measurements of water on Ar−P-exposed NAA membranes at one instant (PDF)

AUTHOR INFORMATION

Corresponding Author

Saleem Shaik − *Department of Physics, IIT Kanpur, Kanpur 208016, India;* orcid.org/0009-0006-5632-943X; Phone: + 91 (0)512 6796601; Email: saleemsk@iitk.ac.in, saleems.iitk@gmail.com; Fax: + 91 (0)512 6797408

Authors

Prashant Kumar Gupta − *Department of Chemical Engineering, IIT Jodhpur, Jodhpur 342002, India;* orcid.org/0000-0002-4000-0940

Meenaxi Sharma − *Department of Physics, IIT Kanpur, Kanpur 208016, India*

Krishnacharya Khare − *Department of Physics, IIT Kanpur, Kanpur 208016, India;* orcid.org/0000-0001-5669-5858

S. Anantha Ramakrishna − *Department of Physics, IIT Kanpur, Kanpur 208016, India*

Complete contact information is available at: https://pubs.acs.org/10.1021/acsomega.4c07796

Notes

The authors declare no competing financial interest.

ACKNOWLEDGMENTS

The authors acknowledge the funding support from SERB, New Delhi, Project no. CRG-2019-000915. The authors thank technicians D.D. Pal and Deepali Ubale of Advanced Center for Materials Science, Indian Institute of Technology (IIT) Kanpur, for XPS characterization, and Advanced Imaging Center for AFM characterization, IIT Kanpur. The authors also acknowledge Prof. Y. N. Mohapatra of Physics Dept. and Dr. Prabhat Kumar Dwivedi (a chief scientist at Nano Center) at IIT Kanpur to provide funding for the AFM facility. The authors are grateful to retired Prof. Jitendra Kumar of IIT Kanpur and Prof. D S Patil of IIT Bombay for their valuable discussions. The authors would like to thank Prof. Manindra Agarwal, computer science and engineering department, respected Director IIT Kanpur, for funding to cover publication charges.

REFERENCES

(1) De Gennes, P.-G. Wetting: statics and dynamics. *Rev. Mod. Phys.* **1985**, *57*, 827−863.

(2) Cassie, A.; Baxter, S. Wettability of porous surfaces. *Trans. Faraday Soc.* **1944**, *40*, 546−551.

(3) Zhang, W.; Huang, L.; Zi, C.; Cai, Y.; Zhang, Y.; Zhou, X.; Shang, F.; Zhao, L.; Liu, Y.; Li, G. Wettability of porous anodic aluminium oxide membranes with three-dimensional, layered nanostructures. *J. Porous Mater.* **2018**, *25*, 1707−1714.
(4) Kim, S.; Choi, H.; Polycarpou, A. A.; Liang, H. Morphology-influenced wetting model of nanopore structures. *Friction* **2016**, *4*, 249−256.
(5) Zgura, I.; Frunza, S.; Frunza, L.; Enculescu, M.; Florica, C.; Cotorobai, F.; Ganea, P. Polyester fabrics covered with amorphous titanium dioxide layers: Combining wettability measurements and photoinduced hydrophilicity to assess their surface properties. *Rom. Rep. Phys.* **2016**, *68*, 259−269.
(6) Miller, J. D.; Veeramasuneni, S.; Drelich, J.; Yalamanchili, M. R.; Yamauchi, G. Effect of roughness as determined by atomic force microscopy on the wetting properties of PTFE thin films. *Polym. Eng. Sci.* **1996**, *36*, 1849−1855.
(7) Papadopoulou, E.; Zorba, V.; Pagkozidis, A.; Barberoglou, M.; Stratakis, E.; Fotakis, C. Reversible wettability of ZnO nanostructured thin films prepared by pulsed laser deposition. *Thin Solid Films* **2009**, *518*, 1267−1270.
(8) Popescu, A.; Duta, L.; Dorcioman, G.; Mihailescu, I.; Stan, G.; Pasuk, I.; Zgura, I.; Beica, T.; Enculescu, I.; Ianculescu, A.; Dumitrescu, I. Radical modification of the wetting behavior of textiles coated with ZnO thin films and nanoparticles when changing the ambient pressure in the pulsed laser deposition process. *J. Appl. Phys.* **2011**, *110*, 1−8.
(9) *Technological Innovations in Sensing and Detection of Chemical, Biological, Radiological, Nuclear Threats and Ecological Terrorism*, 1st ed.; Vaseashta, A., Braman, E., Susmann, P., Garson, A. M., Eds.; Springer: Dordrecht, 2011.
(10) Yamamoto, O. Influence of particle size on the antibacterial activity of zinc oxide. *Int. J. Inorg. Chem.* **2001**, *3*, 643−646.
(11) Rajendra, R.; Balakumar, C.; Ahammed, H. M.; Jayakumar, S.; Vaideki, K.; Rajesh, E. Use of zinc oxide nano particles for production of antimicrobial textiles. *IJEST* **2010**, *2*, 202−208.
(12) Brayner, R.; Ferrari-Iliou, R.; Brivois, N.; Djediat, S.; Benedetti, M. F.; Fiévet, F. Toxicological Impact Studies Based on Escherichia coli Bacteria in Ultrafine ZnO Nanoparticles Colloidal Medium. *Nano Lett.* **2006**, *6*, 866−870.
(13) Yamamoto, O.; Komatsu, M.; Sawai, J.; Nakagawa, Z.-e. Effect of lattice constant of zinc oxide on antibacterial characteristics. *J. Mater. Sci.: Mater. Med.* **2004**, *15*, 847−851.
(14) Huang, Z.; Zheng, X.; Yan, D.; Yin, G.; Liao, X.; Kang, Y.; Yao, Y.; Huang, D.; Hao, B. Toxicological effect of ZnO nanoparticles based on bacteria. *Langmuir* **2008**, *24*, 4140−4144.
(15) Textor, T.; Mahltig, B. A sol−gel based surface treatment for preparation of water repellent antistatic textiles. *Appl. Surf. Sci.* **2010**, *256*, 1668−1674.
(16) Alongi, J.; Tata, J.; Frache, A. Hydrotalcite and nanometric silica as finishing additives to enhance the thermal stability and flame retardancy of cotton. *Cellulose* **2011**, *18*, 179−190.
(17) Bahners, T. The Do's and Don'ts of Wettability Characterization in Textiles. *J. Adhes. Sci. Technol.* **2011**, *25*, 2005−2021.
(18) Karmi, A.; Sakala, G. P.; Rotem, D.; Reches, M.; Porath, D. Durable, stable, and functional nanopores decorated by self-assembled dipeptides. *ACS Appl. Mater. Interfaces* **2020**, *12*, 14563−14568.
(19) Zheng, D.; Choi, C.-H.; Sun, G.; Zhao, X. Superwicking on Nanoporous Micropillared Surfaces. *ACS Appl. Mater. Interfaces* **2020**, *12*, 30925−30931.
(20) Guo, T.; Oztug, N. A. K.; Han, P.; Ivanovski, S.; Gulati, K. Old is gold: electrolyte aging influences the topography, chemistry, and bioactivity of anodized TiO2 nanopores. *ACS Appl. Mater. Interfaces* **2021**, *13*, 7897−7912.
(21) Jiao, X.; Li, Y.; Li, F.; Sun, R.; Wang, W.; Wen, Y.; Song, Y.; Zhang, X. Voltage-responsive controlled release film with cargo release self-monitoring property based on hydrophobicity switching. *ACS Appl. Mater. Interfaces* **2017**, *9*, 10992−10999.
(22) Chen, Q. Enhanced Fluid Flow through Nanopores by Polymer Brushes. *Langmuir* **2014**, *30*, 8119−8123.
(23) de Groot, G. W.; Santonicola, M. G.; Sugihara, K.; Zambelli, T.; Reimhult, E.; Vörös, J.; Vancso, G. J. Switching transport through nanopores with pH-responsive polymer brushes for controlled ion permeability. *ACS Appl. Mater. Interfaces* **2013**, *5*, 1400−1407.
(24) Frament, C. M.; Bandara, N.; Dwyer, J. R. Nanopore surface coating delivers nanopore size and shape through conductance-based sizing. *ACS Appl. Mater. Interfaces* **2013**, *5*, 9330−9337.
(25) Feng, X.; Mei, S.; Jin, Z. Wettability transition induced transformation and entrapment of polymer nanostructures in cylindrical nanopores. *Langmuir* **2011**, *27*, 14240−14247.
(26) Shaat, M. Viscosity of water interfaces with hydrophobic nanopores: application to water flow in carbon nanotubes. *Langmuir* **2017**, *33*, 12814−12819.
(27) Liu, L.; Zhao, J.; Culligan, P. J.; Qiao, Y.; Chen, X. Thermally responsive fluid behaviors in hydrophobic nanopores. *Langmuir* **2009**, *25*, 11862−11868.
(28) Chen, X.; Zhang, S.; Hou, D.; Duan, H.; Deng, B.; Zeng, Z.; Liu, B.; Sun, L.; Song, R.; Du, J.; et al. Tunable Pore Size from Sub-Nanometer to a Few Nanometers in Large-Area Graphene Nanoporous Atomically Thin Membranes. *ACS Appl. Mater. Interfaces* **2021**, *13*, 29926−29935.
(29) Lim, H. S.; Kwak, D.; Lee, D. Y.; Lee, S. G.; Cho, K. UV-driven reversible switching of a roselike vanadium oxide film between superhydrophobicity and superhydrophilicity. *J. Am. Chem. Soc.* **2007**, *129*, 4128−4129.
(30) Myint, M. T. Z.; Kumar, N. S.; Hornyak, G. L.; Dutta, J. Hydrophobic/hydrophilic switching on zinc oxide micro-textured surface. *Appl. Surf. Sci.* **2013**, *264*, 344−348.
(31) Miyauchi, M.; Kieda, N.; Hishita, S.; Mitsuhashi, T.; Nakajima, A.; Watanabe, T.; Hashimoto, K. Reversible wettability control of TiO2 surface by light irradiation. *Surf. Sci.* **2002**, *511*, 401−407.
(32) Thiam, E. h. Y.; Dramé, A.; Sow, S.; Sene, A.; Szczepanski, C. R.; Dieng, S. Y.; Guittard, F.; Darmanin, T. Designing Nanoporous Membranes through Templateless Electropolymerization of Thieno-[3,4-b]thiophene Derivatives with High Water Content. *ACS Omega* **2019**, *4*, 13080−13085.
(33) Megias-Alguacil, D.; Tervoort, E.; Cattin, C.; Gauckler, L. J. Contact angle and adsorption behavior of carboxylic acids on α-Al2O3 surfaces. *J. Colloid Interface Sci.* **2011**, *353*, 512−518.
(34) Norek, M.; Krasińsk, A. Controlling of water wettability by structural and chemical modificationof porous anodic alumina (PAA): Towards super-hydrophobic surfaces. *Surf. Coat. Technol.* **2015**, *276*, 464−470.
(35) Yamamoto, Y.; Baba, N. Nature of the carboxylate species incorporated in anodic alumina films formed in oxalic acid solution. *Thin Solid Films* **1983**, *101*, 329−338.
(36) Rauf, A.; Mehmood, M.; Ahmed, M.; ul Hasan, M.; Aslam, M. Effects of ordering quality of the pores on the photoluminescence of porous anodic alumina prepared in oxalic acid. *J. Lumin.* **2010**, *130*, 792−800.
(37) Vrublevsky, I.; Chernyakova, K.; Ispas, A.; Bund, A.; Gaponik, N.; Dubavik, A. Photoluminescence properties of heat-treated porous alumina films formed in oxalic acid. *J. Lumin.* **2011**, *131*, 938−942.
(38) Huang, G.; Wu, X.; Mei, Y.; Shao, X. F.; Siu, G. G. Strong blue emission from anodic alumina membranes with ordered nanopore array. *J. Appl. Phys.* **2003**, *93*, 582−585.
(39) Du, Y.; Cai, W.; Mo, C.; Chen, J.; Zhang, L.; Zhu, X. Preparation and photoluminescence of alumina membranes with ordered pore arrays. *Appl. Phys. Lett.* **1999**, *74*, 2951−2953.
(40) Gao, T.; Meng, G.; Zhang, L. Blue luminescence in porous anodic alumina films: the role of the oxalic impurities. *J. Phys.: Condens. Matter* **2003**, *15*, 2071−2079.
(41) Singh, S. K.; Khandekar, S.; Pratap, D.; Ramakrishna, S. A. Wetting dynamics and evaporation of sessile droplets on nano-porous alumina surfaces. *Colloids Surf., A* **2013**, *432*, 71−81.
(42) Ran, C.; Ding, G.; Liu, W.; Deng, Y.; Hou, W. Wetting on nanoporous alumina surface: transition between Wenzel and Cassie states controlled by surface structure. *Langmuir* **2008**, *24*, 9952−9955.

https://doi.org/10.1021/acsomega.4c07796
ACS Omega 2025, 10, 17170−17181

(43) Li, Z.; Wang, J.; Zhang, Y.; Wang, J.; Jiang, L.; Song, Y. Closed-air induced composite wetting on hydrophilic ordered nanoporous anodic alumina. *Appl. Phys. Lett.* **2010**, *97*, 233107.
(44) Yang, J.; Wang, J.; Wang, C.-W.; He, X.; Li, Y.; Chen, J.-B.; Zhou, F. Intermediate wetting states on nanoporous structures of anodic aluminum oxide surfaces. *Thin Solid Films* **2014**, *562*, 353−360.
(45) Lee, K.; Leese, H.; Mattia, D. Water flow enhancement in hydrophilic nanochannels. *Nano Scale* **2012**, *4*, 2621−2627.
(46) Buijnsters, J. G.; Zhong, R.; Tsyntsaru, N.; Celis, J.-P. Surface Wettability of Macroporous Anodized Aluminum Oxide. *ACS Appl. Mater. Interfaces* **2013**, *5*, 3224−3233.
(47) Yao, L.; Zheng, M.; Ma, L.; Li, W.; Li, M.; Shen, W. Self-assembly of diverse alumina architectures and their morphology-dependent wettability. *Mater. Res. Bull.* **2011**, *46*, 1403−1408.
(48) Mateo, J.; Kulkarni, S.; Das, L.; Bandyopadhyay, S.; Tepper, G.; Wynne, K.; Bandyopadhyay, S. Wetting behavior of polymer coated nanoporous anodic alumina films: transition from super-hydrophilicity to super-hydrophobicity. *Nanotechnology* **2010**, *22*, 035703.
(49) Ye, J.; Yin, Q.-M.; Zhou, Y. Superhydrophilicity of anodic aluminum oxide films: From "honeycomb" to "bird's nest. *Thin Solid Films* **2009**, *517*, 6012−6015.
(50) Kong, J.; Yung, K. L.; Xu, Y.; Tian, W. Wettability transition of plasma-treated polystyrene micro/nano pillars-aligned patterns. *EXPRESS Polym. Lett.* **2010**, *4*, 753−762.
(51) Kim, S.; Kafi, A.; Bafekpour, E.; Lee, Y.; Fox, B.; Hussain, M.; Choa, Y.-H. Wettability Investigation of UV/O_3 and Acid Functionalized MWCNT and MWCNT/PMMA Nanocomposites by Contact Angle Measurement. *J. Nanomater.* **2015**, *2015*, 1−13.
(52) Alam, A. U.; Howlader, M.; Deen, M. The effects of oxygen plasma and humidity on surface roughness, water contact angle and hardness of silicon, silicon dioxide and glass. *J. Manuf. Syst.* **2014**, *24*, 035010.
(53) Montero, C.; Ramírez, C. G.; Muñoz, L.; Sancy, M.; Azócar, M.; Flores, M.; Artigas, A.; Zagal, J. H.; Zhou, X.; Monsalve, A.; et al. Effect of Plasma Argon Pretreatment on the Surface Properties of AZ31 Magnesium Alloy. *Materials* **2023**, *16*, 2327.
(54) Samad, M.; Nayan, N.; Bakar, A.; Wageh, A.; Hamzah, A.; Latif, R. Aluminium Thin Film Surface Modification via Low-Pressure and Atmospheric-Pressure Argon Plasma Exposure. *J. Surf. Invest.: X-Ray, Synchrotron Neutron Tech.* **2022**, *16*, 421−426.
(55) Zhang, J.; Zhou, W.; Chan-Park, M. B.; Conner, S. Argon Plasma Modification of SU-8 for Very High Aspect Ratio and Dense Copper Electroforming. *J. Electrochem. Soc.* **2005**, *152*, C716−C721.
(56) Shaik, S.; Tiwari, A. K.; Ramakrishna, S. A. Alcohol sensor based on gold-coated nanoporous anodic alumina membrane. *Pramana* **2019**, *93*, 30.
(57) Masuda, H.; Fukuda, K. Ordered Metal Nanohole Arrays Made by a Two-Step Replication of Honeycomb Structures of Anodic Alumina. *Science* **1995**, *268*, 1466−1468.
(58) Han, C. Y.; Willing, G. A.; Xiao, Z.; Wang, H. H. Control of the anodic aluminum oxide barrier layer opening process by wet chemical etching. *Langmuir* **2007**, *23*, 1564−1568.
(59) Nečas, D.; Valtr, M.; Klapetek, P. How levelling and scan line corrections ruin roughness measurement and how to prevent it. *Sci. Rep.* **2020**, *10*, 15294.
(60) Nečas, D.; Klapetek, P. One-dimensional autocorrelation and power spectrum density functions of irregular regions. *Ultramicroscopy* **2013**, *124*, 13−19.
(61) Smith, J. R.; Breakspear, S.; Campbell, S. A. AFM in surface finishing: Part II. Surface roughness. *Trans. IMF* **2003**, *81*, B55−B58.
(62) Adamson, A. W.; Gast, A. P.; et al. *Physical Chemistry of Surfaces; Section II*; Interscience Publishers: New York, 1967; Vol. *150*. Chapter 4.
(63) Sowell, R. R.; Cuthrell, R. E.; Mattox, D. M.; Bland, R. D. Surface cleaning by ultraviolet radiation. *J. Vac. Sci. Technol.* **1974**, *11*, 474−475.
(64) Vig, J.; LeBus, J. UV/ozone cleaning of surfaces. *IEEE Trans. Parts, Hybrids, Packag.* **1976**, *12*, 365−370.
(65) Vig, J. R. UV/ozone cleaning of surfaces. *J. Vac. Sci. Technol., A* **1985**, *3*, 1027−1034.
(66) Sham, M. L.; Li, J.; Ma, P. C.; Kim, J.-K. Cleaning and functionalization of polymer surfaces and nanoscale carbon fillers by UV/ozone treatment: a review. *J. Compos. Mater.* **2009**, *43*, 1537−1564.
(67) Luo, Y.-R. *Handbook of Bond Dissociation Energies in Organic Compounds*; CRC Press, 2002.
(68) Farr, N.; Thanarak, J.; Schäfer, J.; Quade, A.; Claeyssens, F.; Green, N.; Rodenburg, C. Understanding surface modifications induced via argon plasma treatment through secondary electron hyperspectral imaging. *Advanced Science* **2021**, *8*, 2003762.
(69) Yamamoto, M.; Matsumae, T.; Kurashima, Y.; Takagi, H.; Suga, T.; Itoh, T.; Higurashi, E. Comparison of argon and oxygen plasma treatments for ambient room-temperature wafer-scale au−au bonding using ultrathin au films. *Micromachines* **2019**, *10*, 119.
(70) Chen, F. F.; et al. *Introduction to Plasma Physics and Controlled Fusion*; Springer, 1984; Vol. *1*.

https://doi.org/10.1021/acsomega.4c07796
ACS Omega 2025, 10, 17170−17181